Nuclear Inst. and Methods in Physics Research, A 1050 (2023) 168136

Contents lists available at ScienceDirect

Nuclear Inst. and Methods in Physics Research, A

journal homepage: www.elsevier.com/locate/nima

Full Length Article

Effect of different scintillator choices on the X-ray imaging performance of CMOS sensors

Rimcy Palakkappilly Alikunju [a,*], Stephen Kearney [a], Robert Moss [a], Asmar Khan [b], Yiannis Stamatis [b], Edward Bullard [b], Thalis Anaxagoras [b], James Brodrick [b], Alessandro Olivo [a]

[a] UCL Department of Medical Physics and Biomedical Engineering, Malet Place, London WC1E 6BT, UK
[b] ISDI Ltd, Highgate Business Centre, 33 Greenwood Place, London NW5 1LB, UK

ARTICLE INFO

Keywords:
CMOS APS
Fibre optic plate (FOP)
Air kerma
Scintillator
pMTF
DQE

ABSTRACT

The ability of wafer scale Complementary Metal Oxide Semiconductor (CMOS) imagers to integrate sensing with analogue to digital conversion at the pixel level has led to their widespread appeal in a variety of imaging applications. This has led to significant improvement in speed and reduction in read-out noise in these imagers when compared to charge-coupled devices (CCDs) and amorphous silicon/selenium based flat panel imagers (FPIs). This paper compares the performance characteristics of CMOS X-ray detectors in various configurations by varying certain parameters of a typical X-ray detector such as fibre optic face plate (FOP), scintillator substrate coating, sensor pixel pitch and scintillator thickness. The evaluations were carried out using RQA5 (70 kV) radiation beam quality aimed at general radiography applications. At comparable Air Kerma values, detectors with a fibre optic plate showed an overall better DQE performance at most spatial frequencies, starting slightly lower at low frequencies then overtaking the "no-FOP" case at mid and high frequencies. The analysis of detectors with different substrate coatings for the scintillators showed comparatively higher DQE for the white-coated aluminium substrate scintillator compared to the black-coated one. The DQE comparison of detectors with 50 μm and 100 μm pixel pitch resulted in a higher DQE for the 100 μm pixel pitch one, with the caveat that the scintillator was thick enough as to render differences in pMTF negligible. Finally, the comparison of scintillators with varying thicknesses showed that the thickest scintillator yielded the highest DQE. These characterisation studies helped in understanding the suitability of these different configurations in various general radiography application scenarios and could be of help to prospective users to determine the overall configuration that best fits their specific imaging needs.

1. Introduction

In recent years, wafer scale Complementary Metal Oxide Semiconductor (CMOS) active pixel sensors (APSs) based X-ray imagers have been widely used in bio-medical applications and beyond [1–8]. These sensors have emerged as an alternative to amorphous silicon or selenium flat panel imagers (FPIs) and charge-coupled devices (CCDs) [2,3].

The main advantages of CMOS sensors are low read noise (60–150e^-), high frame rate, high spatial resolution, low power consumption, and low-cost mass production capability [2–4,6,7,9]. Their competitors such as amorphous Si suffer from higher read noise (>1000e^-), lower frame rate and reduced spatial resolution due to a typically larger pixel pitch [2,10], whereas CCDs have high production cost and are physically small (e.g., 2–4 cm^2), hence demagnification is needed to access larger fields of view. Nevertheless, the demagnification raises the possibility of a secondary quantum sink to maintain acceptable levels of image quality [3,11]. Some of the weakest points of CMOS sensors are the limited radiation hardness and the size of the single imager tile [6]. However, stitching and tiling methods can be applied to create sensors with areas sufficiently large to be suitable for medical X-ray imaging applications [3,12].

This paper reports on X-ray characterisation studies performed on CMOS based indirect conversion detectors manufactured at ISDI [13], a CMOS image sensor manufacturer based in London. The studied detectors were mainly aimed at dental, Non Destructive Testing (NDT), Industrial CT, and fluoroscopy applications. In particular, we studied the effects that certain changes in configuration have on the overall X-ray performance of the detector, namely (i) using a fibre optic plate (FOP) versus not using it, (ii) having different substrate coatings for the scintillators, (iii) using sensors with different pixel pitches, and finally (iv) using scintillators of different thicknesses.

The performance evaluation was based on the extraction of X-ray characterisation metrics such as sensitivity, presampling modulation

* Corresponding author.
E-mail address: rimcy.alikunju.19@ucl.ac.uk (R.P. Alikunju).

https://doi.org/10.1016/j.nima.2023.168136
Received 12 December 2022; Received in revised form 10 February 2023; Accepted 10 February 2023
Available online 13 February 2023

Table 1
Sensor specifications.

Sensor	Technology	Pixel pitch (μm)	Image size
Sensor 1	CMOS APS	50	2802 x 2400
Sensor 2	CMOS APS	100	1402 x 1200
Sensor 3	CMOS APS	100	2063 x 2049

transfer function (pMTF), noise power spectrum (NPS), and detective quantum efficiency (DQE) as per the IEC 62220-1 standard [14] specifications in each case. The pMTF defines the spatial resolution of the detector, i.e., the ability of the detector to identify closely spaced features as distinct, whereas the NPS expresses the distribution of image noise at the various spatial frequency components of the image. The combination of signal to noise ratio (SNR), MTF and NPS determines the DQE, which is a compact expression for the contrast-detail resolution [4]. The radiation beam quality used throughout the study was RQA5(70 kV), aimed at general radiography applications.

2. Materials and methods

The X-ray performance evaluation was performed by using an X-ray source with a tungsten (W) anode placed inside a Faxitron (Hologic, Marlborough, MA) cabinet. In line with the RQA5 (70 kV) radiation beam quality requirements set forth by IEC standards [14], 21 mm external Al filtration was used throughout the measurements; The IEC standards require this is added to simulate the imaged organs [3,15]. The Air-Kerma (K_a, in μGy), measurements at the detector surface were performed with the Inovision 35050A calibrated Ionisation Chamber (IC).

Table 1 shows the specifications of the sensors used for the characterisation studies. Sensor 2 and sensor 3 are manufactured in a similar way and vary only in their dimensions.

Although in principle both Low Full Well (LFW) and High Full Well (HFW) modes of operation were available, this paper addresses only the LFW mode.

All characterised X-ray detectors were coupled to columnar Thallium activated Caesium Iodide (CsI:Tl) scintillators. These scintillators offer high spatial resolution due to the light guiding property of their columnar structures. In most cases, an FOP is inserted between the scintillator and the sensor to prevent direct interaction of X-rays in the sensor. If the scintillator is directly coupled to the detector, radiation can penetrate through it and interact in the sensor itself, with a small number of events producing much large charge quantities thus increasing noise [3,16]. Unless otherwise stated, the FOPs used in the characterised detectors are 2 mm thick, have a numerical aperture (N.A) of 1.0, and include extramural absorbers (EMA fibres).

2.1. Pre-sampling modulation transfer function (pMTF)

The pMTF indicates how efficiently an input signal is transferred to the output image at each spatial frequency. It quantifies the spatial resolution of an imaging system. To calculate the pMTF, the first step is to determine the oversampled Edge Spread Function (ESF). To determine the oversampled ESF, an opaque, polished edge test object (eg: W foil, 1 mm thick) was placed on the detector surface at a shallow angle α, (1.5 to 3 degrees) with respect to the pixel matrix, and images are captured and then corrected for any photo response non-uniformities like gain and offset.

The ESF curves (effectively oversampled edge profiles) were then obtained from N consecutive rows/columns located along the edge. Seven consecutive ESF profiles straddling the dark and bright areas of the edge image are sufficient to reduce the statistical noise [3,17]. These profiles were laterally shifted with respect to the central one so that all curves overlapped closely; they were then averaged to calculate the average oversampled ESF. The oversampled ESF is then differentiated using a [−1, 0, 1] or [−0.5, 0, 0.5] kernel to obtain the oversampled line spread function (LSF) [14]. The modulus of the fast Fourier transform of the oversampled LSF, normalised to one at zero frequency, gives the Modulation Transfer Function (MTF). To avoid aliasing effects, the MTF is calculated up to the Nyquist frequency (F_{NYQ}), yielding the pMTF [18].

2.2. X-ray sensitivity

The average output in Digital Numbers (DN) for a specific K_a value, known as the signal transfer property (STP) [3,17], was utilised to express the X-ray sensitivity of the detector at 70 kV (RQA5). The Air Kerma measurements were obtained by varying the exposure time which can be pre-set via the X-ray source settings and noting the corresponding reading from the calibrated IC. The linearity of the sensor in each case was evaluated by performing a linear regression fit.

2.3. Noise power spectrum

The NPS describes how the noise is transferred by the system at different frequencies. The NPS is performed on a stack of 60 images acquired for each exposure time. The images were first offset and gain corrected. About 40 reference frames corresponding to each exposure were used for gain correction and these images should have as little noise as possible. Due to uncorrelated noise (i.e., error) propagation, 40 reference frames are expected to decrease the NNPS and subsequently the DQE results by ~2.5% [19]. This is acceptable because the IEC standard allows an uncertainty of 5% for NNPS and 10% for the DQE results.

The NPS is calculated from 256*256 Regions of Interest (ROIs), first by moving progressively in the horizontal direction from the top left corner of the image and then in the vertical direction until the end of the image such that every new ROI is overlapped by 128 pixels with the previous one. A second order polynomial fit $S(x_i, y_i)$ was applied to each captured image to correct for any residual backgrounds trends (due to e.g. the heel effect), and subtracted from the flat-field image $I(x_i, y_i)$. The average 2D NPS is then calculated by applying a 2D Fourier transform to each ROI for all the acquired frames as per Eq. (1) [3,4,14]:

$$NPS(u,v) = \frac{\Delta x \Delta y}{M N_x N_y} \sum_{m=1}^{M} \left| FFT\left\{ I(x_i, y_i) - S(x_i, y_i) \right\} \right|^2 \quad (1)$$

where u and v are the spatial frequencies corresponding to x and y, Δx and Δy are the pixel pitches along x and y, N_x and N_y express the ROI size in pixels in the x and y directions, M is the number of ROIs used in the ensemble average, and FFT denotes the fast Fourier transform operation.

Finally, the 1D NPS is extracted from the 2D NPS by averaging seven rows and seven columns on both sides of the corresponding axis, excluding the axis, to provide horizontal and vertical 1D NPSs respectively.

2.4. Detective quantum efficiency (DQE)

The DQE is a frequency dependent measure of the efficiency of an imaging system [20]. It indicates the detector's ability to transfer the signal to noise ratio (SNR) from input to output, i.e., it is an estimate of how effectively it uses the input X-ray quanta. It is given by Eq. (2):

$$DQE(f) = \frac{SNR_{out}^2}{SNR_{in}^2} = \frac{MTF^2(f)}{\frac{\Phi}{K_a}.K_a.NNPS(f)} \quad (2)$$

where $\frac{\varnothing}{k_a}$ is the fluence per Air Kerma, or squared signal to noise ratio (SNR_{in}^2) per Air Kerma given in units of $1/(mm^2 \cdot \mu Gy)$. According to the IEC standard, the SNR_{in}^2 value for the RQA5 beam quality determined using the SPECMAN software is 29653 in units of $1/(mm^2 \cdot \mu Gy)$ [14].

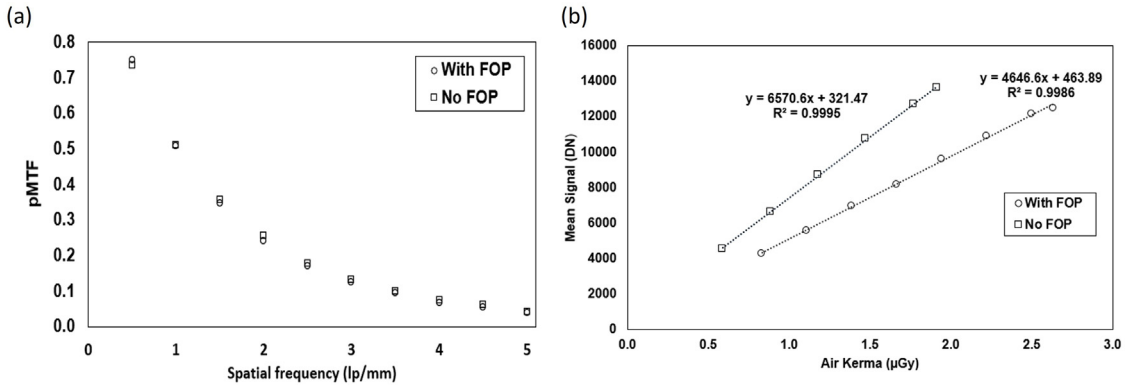

Fig. 1. (a) pMTF comparison for the FOP and no FOP cases. (b) STP curves of the sensors with displayed fitting equations for the FOP and no FOP cases.

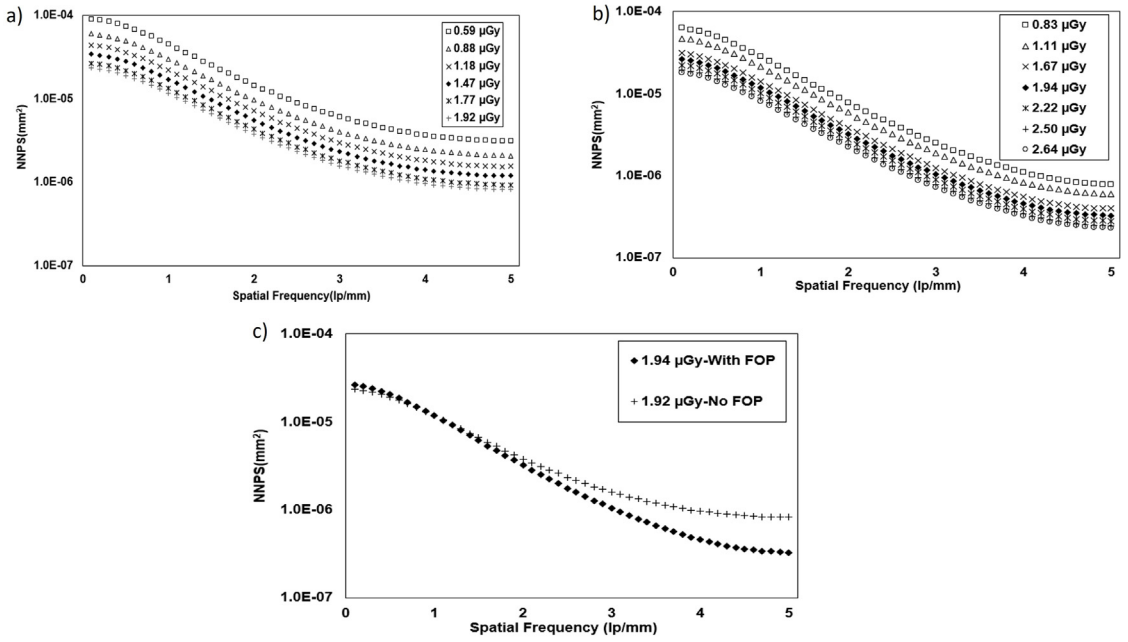

Fig. 2. 1D NNPS at different values of K_a for a sensor without (a) and with (b) an FOP. (c) comparison between the FOP and no FOP cases at similar Air Kerma value.

3. Results and discussions

The pMTF, STP, NPS and DQE evaluation as per the methodology described in Section 2 was performed on a series of X-ray detector configurations while varying a specific parameter each time (specified in the titles of the following sub-sections), to allow for a direct comparison and therefore for an assessment of its effect. The analysis was performed by using software written in MATLAB R2021a.

3.1. X-ray detectors with and without FOP

Firstly, the pMTF of a 100 μm pixel pitch(pp) sensor with and without an FOP was studied. A 600 μm CsI scintillator was used in both cases. As can be seen from Fig. 1(a), the detector without the FOP shows a slightly higher pMTF than that with the FOP (with increases of 3.2%, 6% and 12% at 1.5, 2 and 4 lp/mm, respectively). This is likely due to the additional interface (scintillator/FOP and FOP/sensor as opposed to scintillator/sensor only) which can lead to additional air gaps allowing more light to diffuse laterally. Uneven contacts between different surfaces would also contribute to air gaps. An additional factor could be visible photons hitting the walls of the fibre optics in the FOPs at an angle smaller than the critical angle, thus possibly penetrating sideways into the neighbouring ones. The FOP, however, protects the sensors by blocking the X-rays from reaching its surface, thereby preventing radiation damage, as well as from direct X-ray photon interaction, which would increase noise.

Fig. 1(b) shows the STP curves for the detector with and without FOP. The Air Kerma ranges from 0.59 μGy to 1.92 μGy for the no-FOP case, and from 0.83 μGy to 2.64 μGy for FOP case. An increase in the mean signal is observed in the no FOP case when compared with the FOP case. This is primarily due to the loss of visible photons as they travel through the FOP. Both sensitivity curves are linear, with coefficients of determination R^2 of approximately 0.999.

Fig. 2(a), (b) show the NNPS curves for identical detectors using the same scintillator with and without an FOP. The detector without FOP shows higher noise levels compared to detector with FOP for the same Air Kerma values; this can be better appreciated in the direct comparison at the same Air Kerma shown in Fig. 2(c), although with the caveat that the introduction of the FOP causes the detectors to reach quantum limited behaviour at slightly different Air Kerma levels. The increased noise levels at high spatial frequencies could be caused, among other things, by direct X-ray interactions in the sensor material.

Fig. 3(a) and (b) show DQE curves for X-ray detectors with and without FOP. The DQE (0.1) (i.e., DQE at 0.1 lp/mm) ranges from 0.57 to 0.68 (in the 0.59–1.92 μGy Air Kerma range) and from 0.60 to 0.67 (0.83–2.64 μGy Air Kerma range) without and with the FOP,

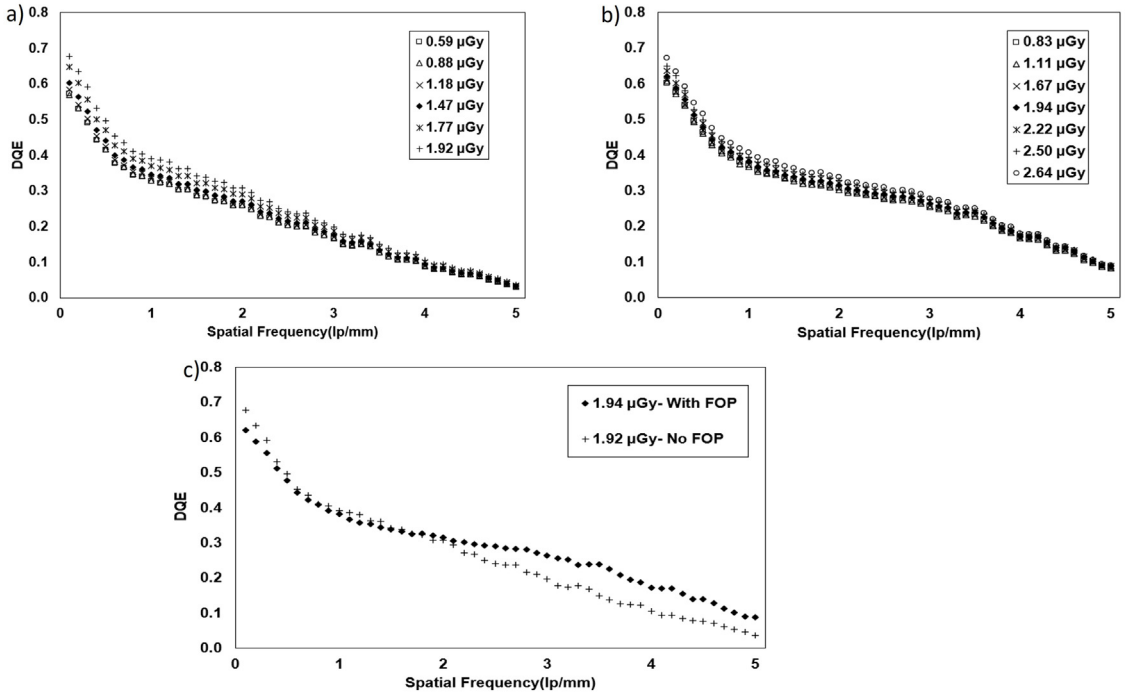

Fig. 3. DQE at 70 kV (RQA5) for a sensor without (a) and with (b) an FOP. (c) comparison between the FOP and no FOP cases at similar Air Kerma value.

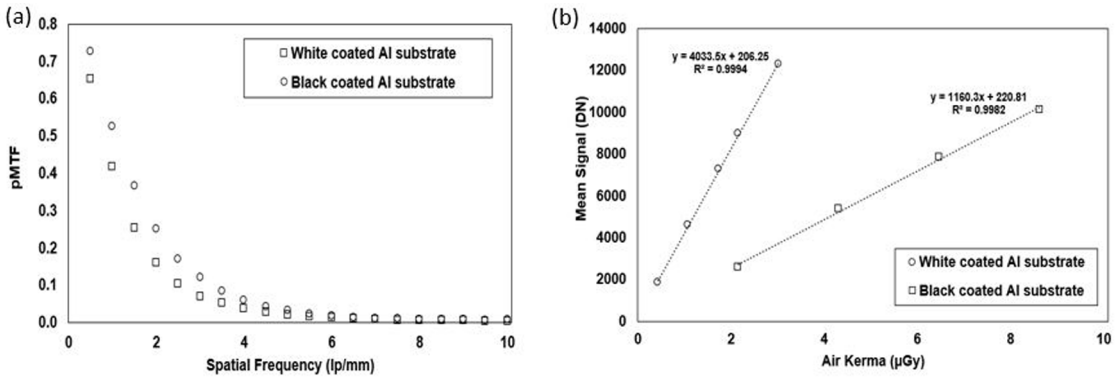

Fig. 4. (a) pMTF comparison for white and black coated scintillator substrates. (b) STP curves of the sensors with displayed fitting equations for white and black coated scintillator substrates.

respectively. Fig. 3(c) shows the direct comparison between DQE curves at a specific Air Kerma value for the sensors with and without the FOP. Overall, the sensor with the FOP has a better DQE performance compared to that without it, which is explained by its better noise performance, especially at mid and higher frequencies.

3.2. X-ray detectors using scintillators with different substrate coatings

In this case, sensor 1 (with a 2 mm FOP) was coupled to 784 µm CsI scintillators with different substrate coatings. Two substrate coatings were used: 0.5 mm white coated aluminium (WCAl), which primarily reflects the backward-transmitted scintillation light that hits it, and 0.3 mm black coated aluminium (BCAl), which largely absorbs it. Reflective coatings, such as the WCAl, maximise the amount of light at the sensors by reducing losses of optical signal from the scintillator [21]. Since the increased light collection of the WCAl arises from increased internal reflection, this is also accompanied by a larger spread of the scintillation light created by individual X-ray photons, and indeed Fig. 4(a) shows a decreased pMTF for the WCAl compared to the BCAl case. At 1 lp/mm, the pMTF of WCAl and BCAl are 41.8% and 52.2% respectively.

Fig. 4(b) shows that, thanks to its reflection property, the scintillator with the WCAl coating is more sensitive than the one using BCAl, with the former providing an approximately 71% increase in light output compared to the latter at the same Air Kerma of 2.16 µGy.

The NNPS curves for the different substrate coatings are shown in Fig. 5(a) and (b), and an NNPS comparison at the same Air Kerma is provided in Fig. 5(c). The direct comparison at the same Air Kerma of 2.16 µGy shows that the detector with black coated scintillator substrate has a higher noise compared to that with the white coated substrate.

Fig. 6(a) and (b) shows the DQE curves corresponding to white and black substrate coating, with the comparison at the same Air Kerma shown in Fig. 6(c). The DQE (0.1) ranges from 0.62 to 0.73 (0.43–3.02 µGy Air Kerma range) and from 0.55 to 0.68 (2.16–8.63 µGy Air Kerma range) with white and black substrate coatings, respectively. The direct comparison shows that the DQE is higher for the white coated substrate scintillator, due to the reduced noise levels compared to the black coated substrate scintillator.

A difference in DQE (0.1) in the two cases can be observed in Fig. 6(c). It should be noted that the X-ray exposure at which the two curves are compared is below the quantum limited regime; at that

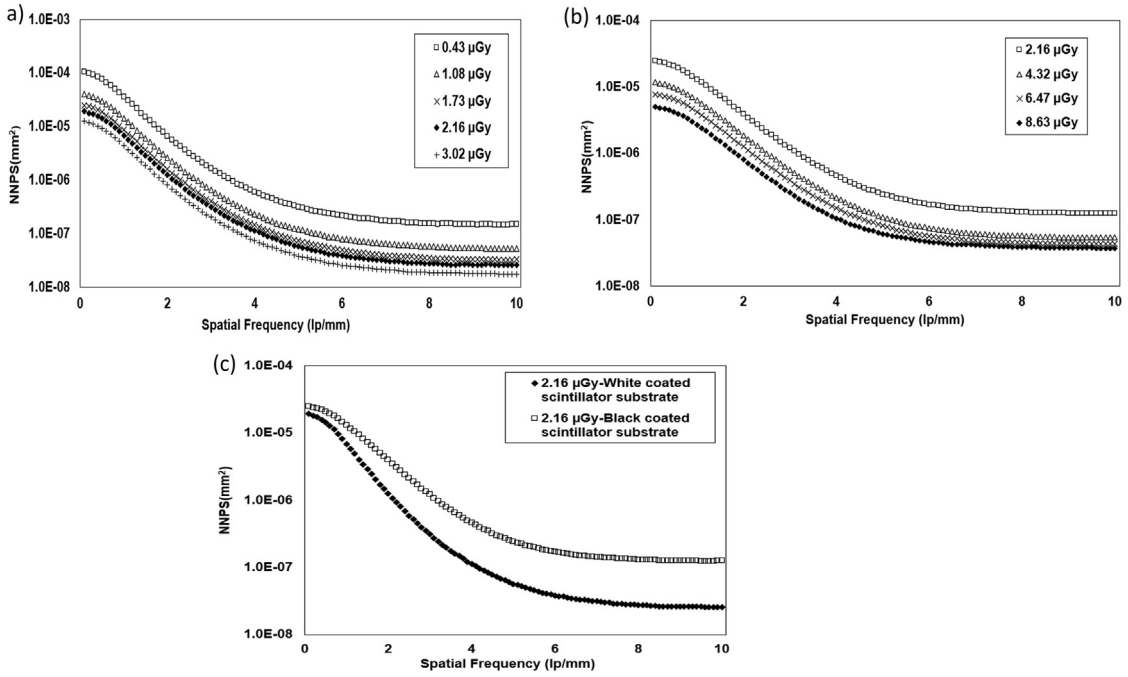

Fig. 5. 1D NNPS at different values of K_a for (a) white-coated substrate scintillator (b) black-coated substrate scintillator (c) comparison between NNPS values for white and black-coated scintillator substrates at similar Air Kerma value.

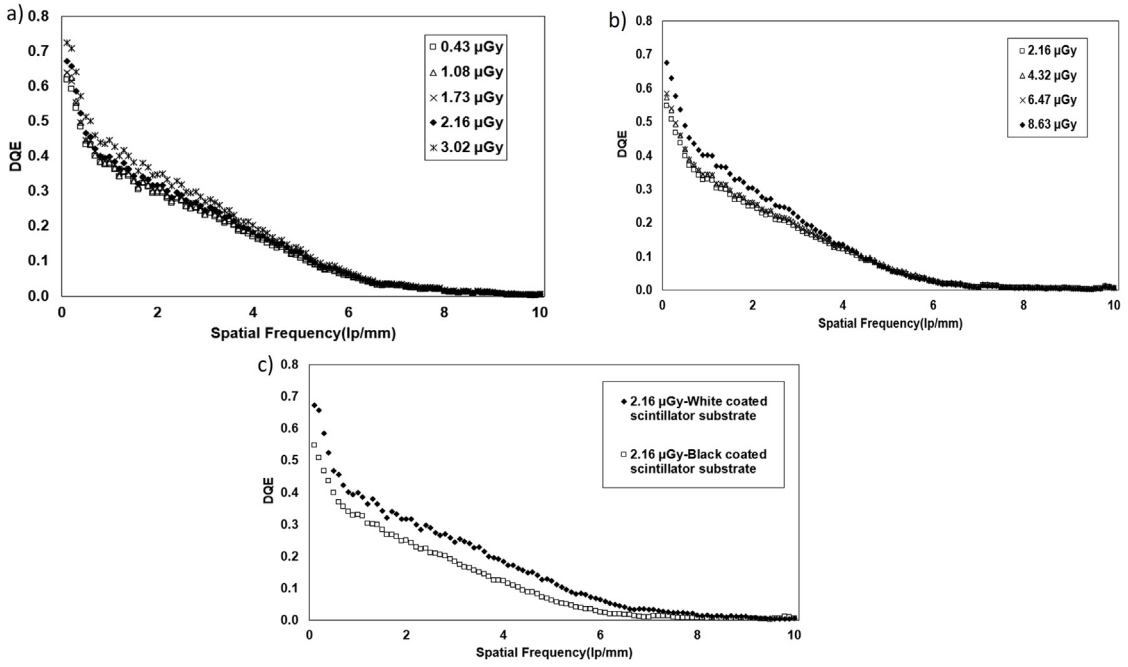

Fig. 6. DQE at 70 kV (RQA5) for (a) white coated Al substrate (b) black coated Al substrate. (c) comparison between white and black coated substrates at a similar Air Kerma value.

exposure, the use of the white coated scintillator results in more visible photons reaching the sensor, effectively corresponding to a "higher X-ray exposure" case for the black coated scintillator as far as the underlying sensor is concerned.

3.3. X-ray detectors with different pixel pitch and same scintillator

In this case, sensors 1 and 2 with a different pixel pitch of 50 µm and 100 µm, with the same FOP and the same scintillator (784 µm CsI with WCAl substrate) were compared. The results shown in Fig. 7(a) demonstrate that, when a scintillator thickness sufficiently larger than the pixel size is employed, the pMTF is not affected by the latter.

Fig. 7(b) shows the STP curves for the two sensors. The Air Kerma ranges between 0.43 and 3.02 µGy for the 50 µm pixel detector, and between 0.43 and 1.08 µGy for 100 µm pixel one. When comparing mean signal values at the identical Air Kerma of 0.43 µGy, the 100 µm pixel detector shows an approximately four times higher sensitivity compared to the 50 µm pixel one (6727 DN versus 1844 DN), as expected due to the ratio between pixel areas. The small deviation is likely due to the different fill factor in the two cases.

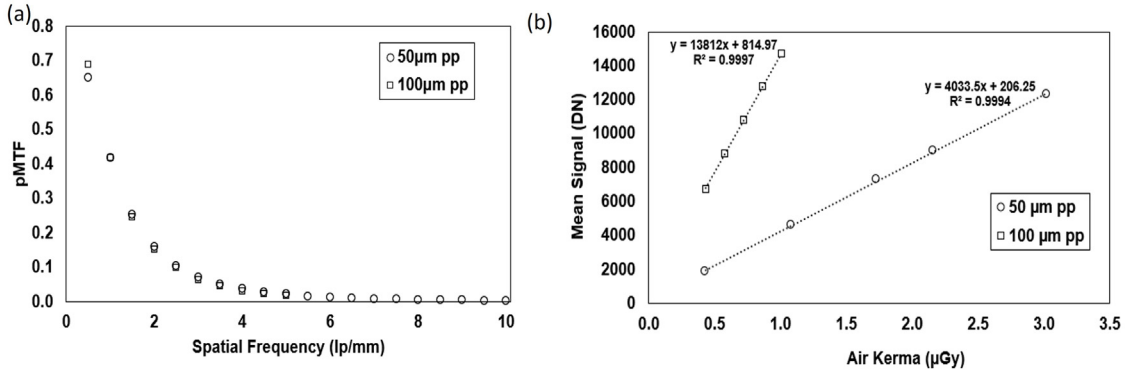

Fig. 7. (a) pMTF comparison for the 50 µm and 100 µm pp sensors. (b) STP curves with displayed fitting equations for the 50 µm and 100 µm pp sensor.

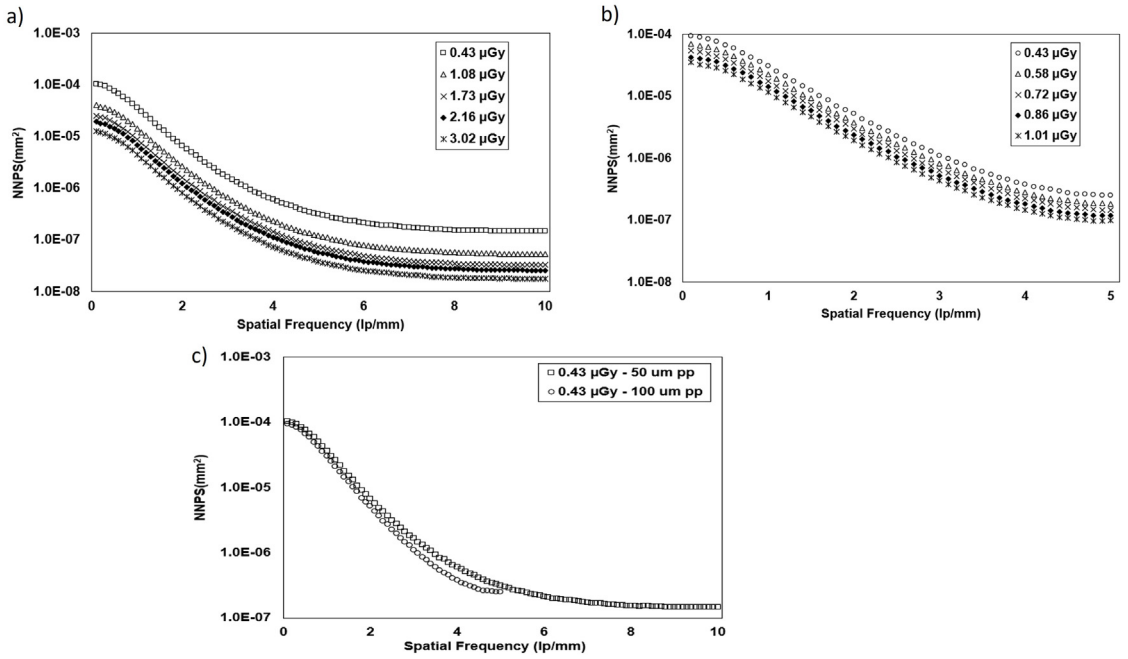

Fig. 8. 1D NNPS at different values of K_a for (a) 50 µm pp sensor and (b) 100 µm pp sensor (c) comparison between the NNPS of the 50 µm and 100 µm pp sensors for similar Air Kerma values.

Fig. 8(a) and (b) shows the NNPS curves for the two pixel sizes. Fig. 8(c) shows a direct NNPS comparison for the two sensors at similar Air Kerma values, showing a better performance for the 100 µm pixel sensor.

Fig. 9(a) and (b) show the DQE as a function of spatial frequency for the two sensors. The DQE (0.1) ranges from 0.62 to 0.73 (0.43–3.02 µGy Air Kerma range) and from 0.76 to 0.86 (0.43–1.01 µGy Air Kerma range) for the 50 µm and 100 µm pixel pitch sensors, respectively. Fig. 9(c) shows that the DQE of the 100 µm pixel pitch sensor is higher than the 50 µm pixel pitch one, since the former has a better NNPS and approximately the same pMTF.

3.4. X-ray detectors with different thickness scintillator

Finally, we studied CMOS Sensor 3 equipped with CsI scintillators of different thicknesses (250 µm, 290 µm and 800 µm) using the same FOP (3 mm thickness, N.A of 1.00 and includes EMA fibres) in all the cases. The 250 µm one used a flexible substrate CsI scintillator whereas the 290 µm and 800 µm were supported on an Al substrate. Importantly, unlike the other two, the 290 µm scintillator used a white coated substrate. The pMTF results are shown in Fig. 10(a). The general trend is a decrease in pMTF as the scintillator thickness increases, due to the correspondingly increased lateral spread of visible light. At 1 lp/mm, pMTF values were 68.6%, 57.7% and 49.2% for the 250 µm, 290 µm and 800 µm scintillators, respectively.

Fig. 10(b) shows the STP curves of the detector for the same sensor/scintillator combinations as in Fig. 10(a), highlighting the trade-off between sensitivity and resolution as the scintillator thickness increases. The graph clearly shows that the mean signal increases with the thickness of the scintillator at the same Air Kerma, in correspondence to its increased X-ray stopping power; for example, the 800 µm scintillator provides the highest sensitivity but also the lowest pMTF values. While in principle one would expect the STP values of the 290 µm scintillator (provided by a different manufacturer) to be closer to the 250 µm than the 800 µm one, this was not observed here, most likely because of the 290 µm scintillator using a white reflective scintillator coating, which was shown above (Fig. 4(b)) to result in a much higher amount of visible photons reaching the sensor surface. Since this also causes more light dispersion, it also explains why the MTF of the 290 µm scintillator is closer to that of the 800 µm rather than the 250 µm one.

Fig. 11(a), (b) and (c) show the average NNPS curves for the three scintillator thicknesses and how these different combinations result in the sensor reaching quantum-limited behaviour at different Air Kerma levels. A comparison of the NNPS curves for the three scintillators at

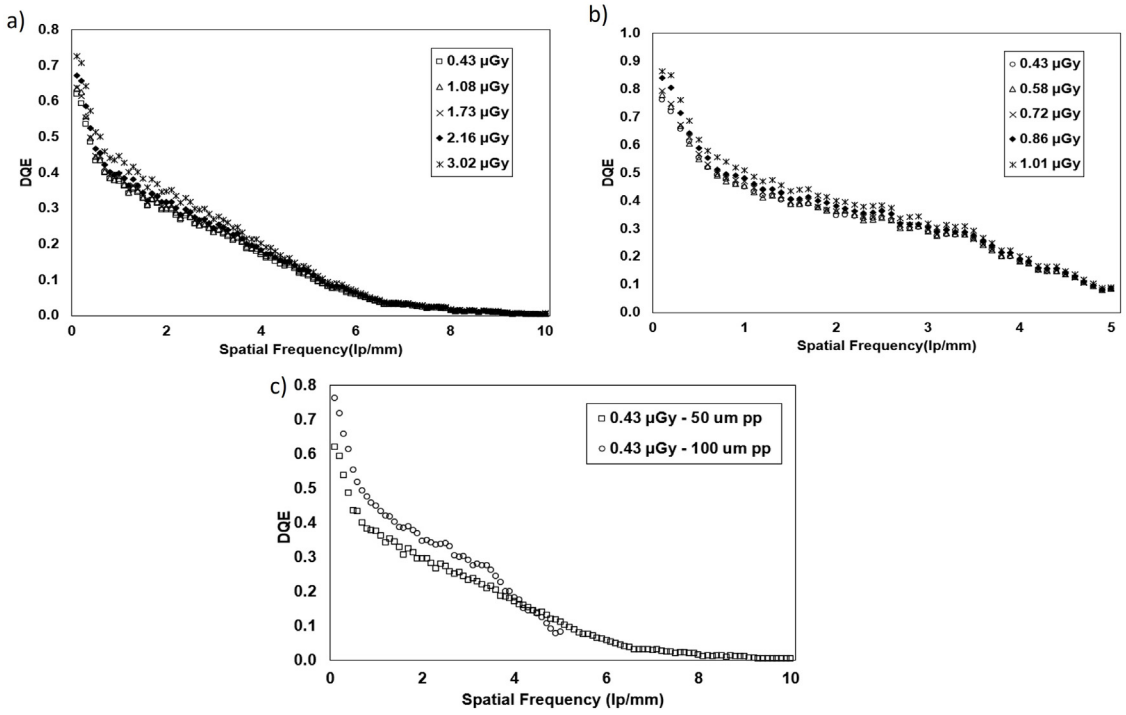

Fig. 9. DQE at 70 kV (RQA5) for (a) 50 µm pp sensor (b) 100 µm pp sensor. (c) comparison between the DQE of the 50 µm and 100 µm pp sensors at similar Air Kerma values.

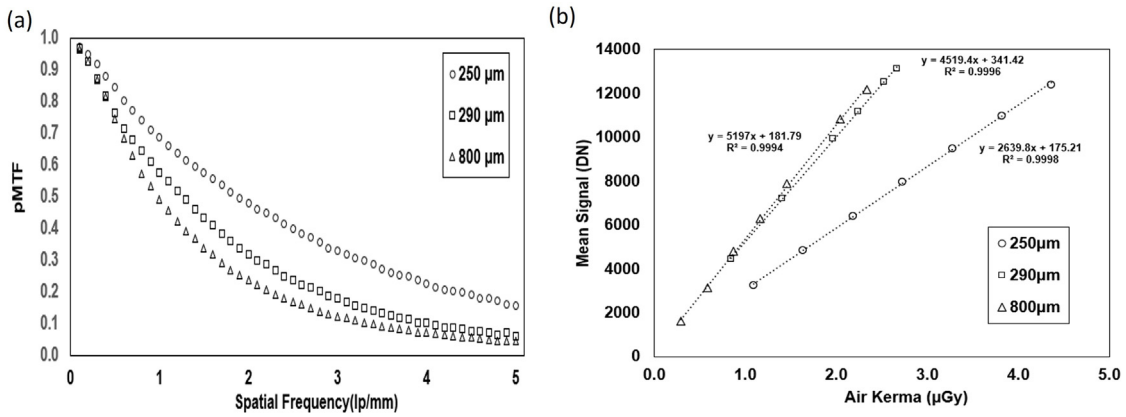

Fig. 10. (a) pMTF comparison for different scintillator thicknesses. (b) STP curves of the sensors with displayed fitting equations for the different scintillator thicknesses.

closest matching Air Kerma values is shown in Fig. 11(d), which shows that the highest and lowest noise levels are observed for the 250 µm and 800 µm scintillators, respectively. Two Air Kerma values are reported for the 800 µm thick scintillator which "bracket" those used in the 250 µm and 290 µm cases, since a closer match was not available.

Fig. 12(a), (b) and (c) show the DQE curves for the sensor coupled to the 250 µm, 290 µm and 800 µm thick CsI scintillators (respectively). The DQE at 0.1 lp/mm ranges from 0.48 to 0.54 (1.09–4.37 µGy Air Kerma range), 0.53 to 0.61 (0.84–2.66 µGy Air Kerma range) and 0.64 to 0.80 (0.29–2.33 µGy Air Kerma range) for the 250 µm, 290 µm and 800 µm thick scintillators, respectively. The 800 µm scintillator shows the highest DQE at low frequency due to its higher X-ray stopping power and therefore higher conversion efficiency.

Fig. 12(d) shows the DQE comparison for the 3 different CsI scintillators at the most similar Air Kerma values that were available (with two values – 2.04 µGy and 2.33 µGy – for the 800 µm thick scintillator for the reasons mentioned above). The 800 µm thick scintillator shows the highest DQE at all spatial frequency for both the 2.04 µGy and 2.33 µGy, indicating that its better noise performance due to higher detection efficiency overcomes the reduction in spatial resolution. Again, when drawing conclusions of this type it should be borne in mind that the detectors obtained through coupling with different scintillators reach quantum-limited behaviour at different Air Kerma values. A thicker scintillator also leads to an improved blocking of direct X-ray hits in the sensor, which can also contribute to reducing noise.

4. Conclusion

The X-ray characterisation studies presented were aimed at understanding the trade-offs in terms of resolution, sensitivity, noise performance and detection efficiency obtained by varying specific detector parameters such as FOP, scintillator substrate coatings, pixel pitch, and scintillator thickness. A direct comparison among the evaluated pMTF, STP, NPS, and DQE showed that:

(i) The sensor without FOP had greater pMTF and sensitivity but a lower DQE compared to the 'with FOP' case.
(ii) For scintillator coatings, the BCAl substrate had better pMTF performance, but the WCAl substrate yielded better sensitivity, noise performance, and detection efficiency.

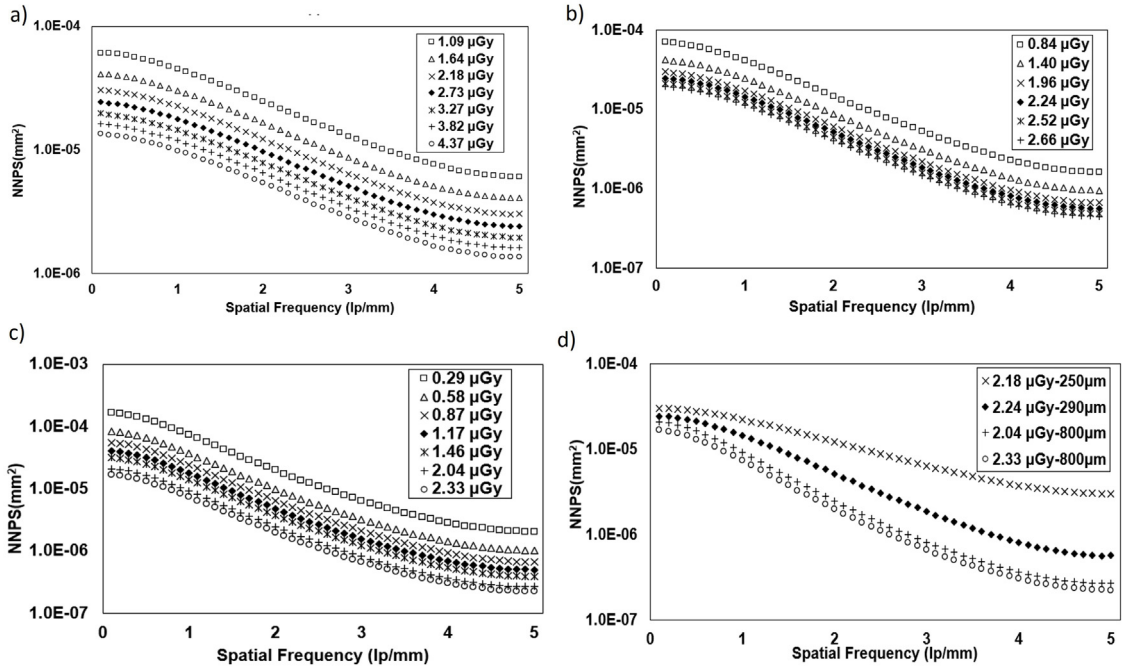

Fig. 11. 1D NNPS at different values of K_a for the 250 µm (a), 290 µm (b) and 800 µm (c) thick CsI scintillators. (d) comparison between NNPS of different scintillators for similar Air Kerma values.

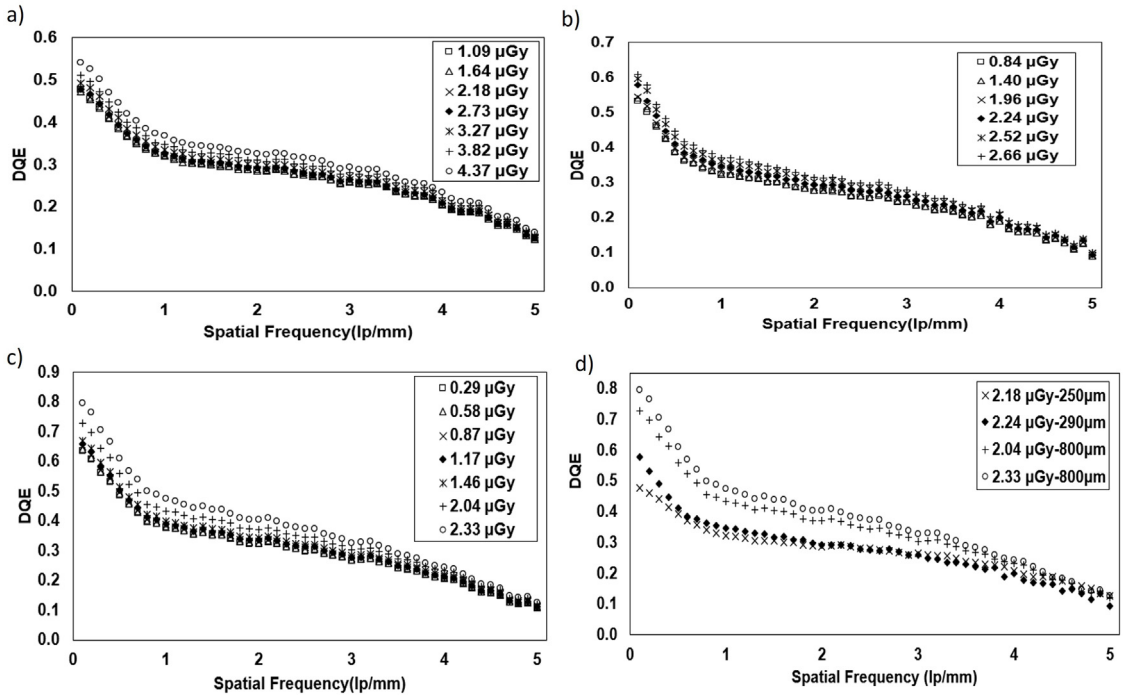

Fig. 12. DQE at 70 kV (RQA5) for the 250 µm (a), 290 µm (b) and 800 µm (c) CsI scintillators. (d) comparison between the DQE of different scintillators for similar Air Kerma values.

(iii) Detectors with 50 µm and 100 µm pixel pitches and a thick (784 µm) scintillator showed identical pMTF, but the 100 µm case demonstrated higher sensitivity, noise performance, and DQE.

(iv) In terms of scintillator thicknesses, the thinnest scintillator (250 µm) had the highest pMTF, whereas the thickest (800 µm) had the highest sensitivity, noise performance, and DQE when compared to other thin scintillators (250 µm and 290 µm).

Based on these characterisation studies, specific X-ray applications can be matched with different detector combinations. For instance, computed tomography (CT) and dental applications demand low Air Kerma, hence detector configurations with high DQE values are preferred. High-resolution detectors with greater pMTFs are preferred for industrial X-ray applications. Thus, this study can help researchers and practitioners choose a detector configuration based on the specific demands of their application.

Declaration of competing interest

The authors declare that they have no known competing financial interests or personal relationships that could have appeared to influence the work reported in this paper.

Data availability

Data will be made available on request.

Acknowledgements

This study is supported by EPSRC (EP/R513143/1 and EP/T005408/1), UK. AO is supported by the Royal Academy of Engineering, UK under their Chair in Emerging Technologies scheme (CiET1819/2/78). The authors would like to thank Dr Anastasios Konstantinidis (Image Quality Specialist at Philips) for useful discussions.

References

[1] B.K. Cha, C.R. Kim, S. Jeon, R.K. Kim, C.W. Seo, K. Yang, D. Heo, T.B. Lee, M.S. Shin, J.B. Kim, O.K. Kwon, X-ray characterization of CMOS imaging detector with high resolution for fluoroscopic imaging application, Nucl. Instrum. Methods Phys. Res. A 731 (2013) 315–319.

[2] M. Esposito, T. Anaxagoras, A.C. Konstantinidis, Y. Zheng, R.D. Speller, P.M. Evans, N.M. Allinson, K. Wells, Performance of a novel wafer scale CMOS active pixel sensor for bio-medical imaging, Phys. Med. Biol. 59 (13) (2014) 3533.

[3] A.C. Konstantinidis, M.B. Szafraniec, R.D. Speller, A. Olivo, The Dexela 2923 CMOS X-ray detector: A flat panel detector based on CMOS active pixel sensors for medical imaging applications, Nucl. Instrum. Methods Phys. Res. A 689 (2012) 12–21.

[4] A. Konstantinidis, Evaluation of Digital X-Ray Detectors for Medical Imaging Applications (Doctoral dissertation), UCL (University College London), 2011.

[5] C.D. Arvanitis, S.E. Bohndiek, G. Royle, A. Blue, H.X. Liang, A. Clark, M. Prydderch, R. Turchetta, R. Speller, Empirical electro-optical and x-ray performance evaluation of CMOS active pixels sensor for low dose, high resolution x-ray medical imaging, Med. Phys. 34 (12) (2007) 4612–4625.

[6] G. Zentai, R. Colbeth, Pros and cons of CMOS X-ray imagers, in: 2012 IEEE International Symposium on Medical Measurements and Applications Proceedings, IEEE, 2012, pp. 1–5.

[7] M. Bigas, E. Cabruja, J. Forest, J. Salvi, Review of CMOS image sensors, Microelectron. J. 37 (5) (2006) 433–451.

[8] M. Shakeri, M. Ariannejad, M. NasimaSedaghati, M. Mamun, S. Amin, Advanced cmos based image sensors, Austr. J. Basic Appl. Sci. 6 (7) (2012) 62–72.

[9] A. El Gamal, H. Eltoukhy, CMOS image sensors, IEEE Circuits Devices Mag. 21 (3) (2005) 6–20.

[10] R.L. Weisfield, N.R. Bennett, Electronic noise analysis of a 127-um pixel TFT/photodiode array, in: Medical Imaging 2001: Physics of Medical Imaging, vol. 4320, SPIE, 2001, pp. 209–218.

[11] M.B. Williams, et al., Analysis of the detective quantum efficiency of a developmental detector for digital mammography, Med. Phys. 26 (1999) 2273–2285.

[12] R. Reshef, T. Leitner, S. Alfassi, E. Sarig, N. Golan, O. Berman, A. Fenigstein, H. Wolf, G. Hevel, S. Vilan, A. Lahav, Large-format medical X-ray CMOS image sensor for high resolution high frame rate applications, in: Proc. Int. Image Sensor Workshop, 2009, pp. 1–4.

[13] ISDI - CMOS image sensor manufacturer, Available at: https://www.isdicmos.com/company. (Accessed 1 December 2022).

[14] International Electrotechnical Commission Publication (IEC62220-1-1), Medical Electrical—Characteristics of Digital X-ray Imaging Devices—Part 1: Determination of the Detective Quantum Efficiency, IEC, 2015.

[15] Samei Ehsan, Performance of digital radiographic detectors: quantification and assessment methods, Adv. Digit. Radiogr.: RSNA 27710 (2003) 37–47.

[16] M.J. Flynn, S.M. Hames, S.J. Wilderman, J.J. Ciarelli, Quantum noise in digital x-ray image detectors with optically coupled scintillators, IEEE Trans. Nucl. Sci. 43 (4) (1996) 2320–2325.

[17] A.C. Konstantinidis, M.B. Szafraniec, L. Rigon, G. Tromba, D. Dreossi, N. Sodini, P.F. Liaparinos, S. Naday, S. Gunn, A. McArthur, R.D. Speller, A. Olivo, X-ray performance evaluation of the dexela CMOS APS x-ray detector using monochromatic synchrotron radiation in the mammographic energy range, IEEE Trans. Nucl. Sci. 60 (5) (2013) 3969–3980.

[18] E. Buhr, S. Günther-Kohfahl, U. Neitzel, Accuracy of a simple method for deriving the presampled modulation transfer function of a digital radiographic system from an edge image, Med. Phys. 30 (9) (2003) 2323–2331.

[19] A.C. Konstantinidis, A. Olivo, R.D. Speller, Modification of the standard gain correction algorithm to compensate for the number of used reference flat frames in detector performance studies, Med. Phys. 38 (12) (2011) 6683–6687.

[20] C. Lawinski, Mackenzie.8 Alistair, Cole Helen, Blake Patricia, Honey Ian, Digital Detectors for General Radiography. A Comparative Technical Report, 2005.

[21] A. Tarancón, E. Marin, J. Tent, G. Rauret, J.F. Garcia, Evaluation of a reflective coating for an organic scintillation detector, Nucl. Instrum. Methods Phys. Res. A 674 (2012) 92–98.